Journal of Solid State Electrochemistry (2025) 29:5173–5186
https://doi.org/10.1007/s10008-025-06365-3

ORIGINAL PAPER

The effects of in-plane strains on the electrochemical properties of Li adatoms on the ZrS_2 monolayer: a first-principles study

B. D. Mahapane[1] · C. Fwalo[1,2] · C. A. Bekeur[1] · R. E. Mapasha[1]

Received: 15 April 2025 / Revised: 13 May 2025 / Accepted: 3 June 2025 / Published online: 9 June 2025
© The Author(s) 2025

Abstract

In this study, we use density functional theory (DFT) with a Hubbard (U) parameter, implemented in the Quantum Espresso code, to investigate the interactions between Li-ions and the ZrS_2 monolayer under the influence of in-plane uniaxial and biaxial strains, specifically within the context of lithium-ion batteries. This is to ensure the ZrS_2 monolayer is more robust against the Coulomb forces arising from interactions between multiple lithium ions. This study objectively examines the impact of tensile and compressive strains ranging from − 5% to 5% on the energetic stability and electrochemical properties of the lithiated ZrS_2 electrode monolayer. For a single Li adatom on a 3×3 ZrS_2 monolayer, the compressed structure (at − 5% strain) becomes more energetically favorable, exhibiting a low adsorption energy of − 1.41 eV. In contrast, the stretched structure (at + 5% strain) has a higher adsorption energy of − 0.95 eV compared to the unstrained structure (− 1.16 eV), although exothermic interaction is maintained. The ZrS_2 electrode monolayer has a shallow energy barrier of 0.23 eV for Li-ion diffusion, indicating greater mobility, which is slightly enhanced by compressive strain. The application of − 5% (compressive strain) resulted in an average OCV of 0.93 V, and 0.78 V for unstrained, while + 5% (tensile strain) yielded an OCV of 0.69 V, which is in the range of commercial anode materials. The tensile strain on a ZrS_2 electrode monolayer would be more effective in mitigating the dendrite formation. The introduction of a Li adatom rearranged the conduction band minimum, leading to the hybridized Zr d orbital states crossing the Fermi level and becoming more populated as the number of Li adatoms increases, leading to a more conductive electrode. Additionally, the strain reduced the band gap, causing the induced electronic states to be continuous from the VBM to the CBM edges, which enhances the electronic conductivity of the material, ensuring the excellent LIBs operation during the charge and discharge processes.

Keywords Density functional theory · Zirconium disulfide · Li adatoms · Tensile and compressive strains · Adsorption energies · Open circuit voltage

Introduction

Recent technological advancements have heightened the urgency to design anode materials for high-performance rechargeable Li-ion batteries (LIBs) [1]. The widely used anode material, graphite, has limitations due to its low theoretical specific capacity of approximately 372 mAh/g [2]. High-performance anode materials should exhibit excellent reversible capacity, strong cycle stability, and high energy density [2–9]. To address the low theoretical specific capacity of graphite, various two-dimensional (2D) materials have been investigated in the search for high-performance anodes [10–16]. In the context of energy storage, significant attention has been given to transition metal dichalcogenide (TMD) monolayers due to their low dimensionality, large surface area, moderate tunable band gap (ranging from 0.1 to 2.0 eV), high electronic mobility, and exceptional mechanical strength. Furthermore, most TMDs can be synthesized using non-complex and low-cost methods [17–19]. A TMD monolayer is made up of three atomic planar layers: an inner transition metal (M) layer is sandwiched in between by the two chalcogen layers to make a hexagonal bent structure.

One of the novel 2D TMDs is the ZrS_2 monolayer, which has been synthesized using various methods [20–24]. It is also a non-toxic material. The most commonly studied

✉ B. D. Mahapane
david.mahapane@up.ac.za

[1] Department of Physics, University of Pretoria, Pretoria, South Africa

[2] Department of Physics, Copperbelt University, Kitwe, Zambia

polymorphs of the ZrS_2 monolayer are 1*H* and 1*T*, which represent distinct geometries, having space groups of $P\bar{6}m2$ and $P\bar{3}m1$, respectively. Several studies indicate that the 1*T* polymorph is the preferred structure in terms of stability [25]. In particular, the ZrS_2 monolayer has a high electronic mobility of 1200 $cm^2\ V^{-1}\ S^{-1}$, significantly higher than other TMDs such as the MoS_2 monolayer (400 $cm^2\ V^{-1}\ S^{-1}$) [21, 26]. The reported electron mobilities indicate that ZrS_2 has lower effective mass and enhanced carrier transport characteristics than MoS_2, suggesting that ZrS_2 is superior for improving performance in various electronic applications. Additionally, the ZrS_2 monolayer is a tunable indirect band gap semiconductor, and its magnitude can be quantified based on the method used, GGA-PBE (≈ 1.1 eV), DFT-PBE +U (≈1.7 eV), HSE06 (≈1.8 eV) [19, 26–29], and experiments (≈1.7 eV) [27, 28, 30]. It was further confirmed that the ZrS_2 monolayer is mechanically and dynamically stable [29]. Based on these findings, concerted efforts by experimentalists and theorists have focused on exploring its practical applications [20, 24, 25, 31].

The ZrS_2 monolayer has been investigated as a suitable anode material. Primarily, during charging, LIBs absorb electrical energy and convert it into chemical energy as stored within the anode materials [32–34]. During discharge, a reduction process occurs in which Li-ions release electrons and become oxidized at the cathode. The released electrons travel through the circuit, attracted towards the positive terminal, generating electrical energy in the process. It was reported that Li binds more strongly with the ZrS_2 monolayer and also has a storage capacity that is higher than that of the MoS_2, SnS_2, and TiS_2 monolayers [25, 35]. Furthermore, the commercially suitable average open circuit voltage of about 0.7 V and excellent migration energy barrier of 0.24 eV are reported [25, 35]. The lithiation of the ZrS_2 monolayer enables a transition from semiconducting to metallic properties due to Li electrons occupying the Zr *d* band [25, 36]. However, it has been reported that achieving 100% reversal of this transition during battery operation is not feasible, unlike in cases where the host material is already metallic. To mitigate this issue, heterolayers consisting of the ZrS_2 monolayer and metallic graphene monolayer were considered [25, 35]. This approach is expected to improve both the conductivity and strength of the materials. Experimental studies by Kim et al. [37] report that an increasing number of Li-ions within the ZrS_2 monolayer lead to strong Coulomb interactions, transforming the ZrS_2 monolayer into an amorphous phase comprising Zr

atoms and Li_2S compounds after discharging to 0.1 V, with this transformation being reversible during charging. These noted setbacks clearly indicate limitations in energy density, charge/discharge rates, and overall cycle life, hindering the potential for high-performance anodes. One way to address these issues and mitigate the failure of the ZrS_2 monolayer anode during lithiation could be the application of in-plane strain engineering.

Strain engineering has played a pivotal role in fine-tuning the properties of 2D materials to meet specific needs [38–40]. Previous studies have reported that 2D materials can sustain extremely high elastic strain conditions before collapsing, as compared to bulk materials [41, 42]. Theoretical computational research can implement in-plane strain by varying the lattice parameters of a material system, while experimental research employs the lattice mismatch technique [30, 43–45]. Previous DFT studies have shown that the application of uniaxial and biaxial strains alters the band gap of ZrS_2 monolayer [19, 46, 47]. It has been reported that both biaxial and uniaxial tensile strains increase the band gap of ZrS_2 monolayer by different magnitudes, while compressive strains decrease it. It is worthwhile to understand the response of Li-ions on the ZrS_2 monolayer under different strain conditions. Specifically, this should focus on the stability and diffusion rate, which contribute to the charging/discharging, when the Coulomb force between Zr and S atoms is altered by tensile or compressive strains. The influence of strain on the metallic character should be carefully examined to determine whether conductivity is enhanced or reduced. Although there is no evidence of the effects of tensile and compressive strains on the electrochemical properties of lithiated ZrS_2 monolayers, such evidence does exist for other monolayers; for example, Hao et al. [48, 49] demonstrated that tensile strains enhance the Li adsorption energy on MoS_2 monolayers, while having minimal influence on the migration energy barriers. At low concentrations, Li adatoms on V_2C and Nb_2C monolayers are stabilized by compressive strain, which significantly reduces the diffusion barriers [40].

In this study, the influence of moderate strain (ranging from −5% (compressive) to +5% strains (tensile)) on Li-ions on the ZrS_2 monolayer was investigated using the DFT approach. This is to ensure the ZrS_2 monolayer is more robust against the Coulomb forces arising from interactions between multiple lithium ions. This aims to enhance the stability, mobility, storage potential, and conductivity of Li-ions on the ZrS_2 monolayer. At this strain range, the single Li adatom on the ZrS_2 structures underwent elastic deformation, ruling out the possibility of immediate amorphization, based on the analyzed strain energy. Based on the adsorption energy analysis of a single Li adsorption, the Li-ZrS_2 structures became more energetically favorable under compressive strain (from −2.5% to −5%) and less favorable as tensile strain increased (from 2.5% to 5%) while maintaining an exothermic reaction. The strain has minimal impact on the energy barriers for Li-ion diffusion, except for a slight reduction under compressive strain. Compressive strain reduced the band gap, causing the induced electronic states with high peaks to be continuous from the VBM to the

CBM edges, thereby enhancing the electronic conductivity of the ZrS_2 structures.

Computational methods

Spin-polarized density functional theory (DFT), implemented within the Quantum Espresso software package [50, 51], is used to optimize the lithium adatoms on the ZrS_2 monolayer structure and to calculate their various properties. The generalized gradient approximation with the Perdew-Burke-Ernzerhof (GGA-PBE) flavor was used to describe the electron exchange-correlation potential [52]. Additionally, electronic spin was assigned to each atom prior to the calculations. To obtain accurate results, convergence tests were conducted for the kinetic energy cut-off used in the expansion of plane waves and for the k-points sampling of the Brillouin zone, generated using the Monkhorst-Pack scheme [53]. An energy cut-off of 500 eV and a 5 × 5 × 1 k-point grid are sufficient to yield accurate results. To account for the interactions between core and valence electrons, ultra-soft pseudopotentials generated from the projector augmented wave (PAW) method were used [54]. The electronic configurations used for constructing the pseudopotentials are as follows: Zr is $4s^2\ 4p^6\ 4d^2\ 5s^2$, S is $3s^2\ 3p^4$, and Li is $2s^1$. The total energies of the ZrS_2 monolayer and Li adsorption on the ZrS_2 monolayer were allowed to converge to within 10^{-6} eV. The Zr, S, and Li atomic positions were allowed to relax until the forces were below 0.02 eV/Å, calculated considering the Hellman–Feynman theorem. The Methfessel-Paxton smearing method [55] was used to set the occupancy of electronic energy states with a spread of 0.02 eV.

In our DFT study, a 1×1 unit of ZrS_2 monolayer was considered, obeying periodic boundary conditions (PBC) [56]. As mentioned in the introduction section, the most commonly studied polymorphs of the ZrS_2 monolayer are 1*H* and 1*T*, which represent distinct geometries, having space groups of $P\bar{6}m2$ and $P\bar{3}m1$, respectively. In the 1H structure, the top and bottom sulfur (S) atoms are directly opposite to each other, and the zirconium (Zr) atoms show trigonal prismatic coordination. In the 1 T structure, the top and bottom S atoms are positioned diagonally, with the Zr atoms showing octahedral coordination. After structural optimization, the calculated cohesive energies defined as the energy required to disassemble the ZrS_2 monolayer into the isolated sulfur (S) and zirconium (Zr) atoms are 5.29 eV/unit cell with a lattice constant of 3.57 Å for the 1H structure and 5.34 eV/unit cell with a lattice constant of 3.66 Å for the 1 T structure. This is an indication that the 1 T structure is the energetically preferred polymorph, in agreement with the previous study [25].

The converged $c = 20$Å value was used, ensuring that the unwanted interaction between the periodic ZrS_2 monolayer images is negligible. The Grimme dispersion correction method (DFT-D3) [57] was applied to the supercell to account for potential van der Waals forces between the Zr and S layers, which could influence the energetic and structural stability of the system. To correct the band gap of ZrS_2 monolayer due to the limitations of the GGA-PBE functional, we applied DFT with a Hubbard-*U* correction. We conducted several tests varying the *U* parameter to identify the value that yields a band gap equivalent to the experimental value of 1.62 eV [27]. The nudged elastic band (NEB) method [58] was employed to examine the minimum energy path (MEP) for Li diffusion across the ZrS_2 monolayer, from one stable adsorption site to another. Additionally, we calculated the adsorption energies E_{ads} of the Li adatoms on the ZrS_2 monolayer to test for the supercell convergence and examine the stability of different sites; this was achieved using the following formula:

$$E_{ads}(Li) = E_{ZrS_2+ad} - E_{ZrS_2} - nE_{Li} \quad (1)$$

The E_{ZrS2}+Li is the total energy of the Li adatoms on the ZrS_2 monolayer, E_{ZrS2} is the total energy of the ZrS_2 monolayer without the Li adatoms, and E_{Li} represents the energy per atom of bulk Li in its stable body-centered cubic (BCC) phase. *n* is the number of Li atoms attached to the ZrS_2 monolayer. The positive $E_{ads}(Li)$ refers to the exothermic adsorption, while the negative $E_{ads}(Li)$ refers to endothermic adsorption. A positive $E_{ads}(Li)$ indicates exothermic adsorption, while a negative $E_{ads}(Li)$ refers to endothermic adsorption. We also investigated the influence of uniaxial and biaxial strains on Li adatoms on the ZrS_2 monolayer. The strain energy, ε, is defined by the following equation:

$$\varepsilon = \frac{a - a_0}{a_0} \times 100\% \quad (2)$$

where α and α_0 refer to the lattice constants of strained and unstrained ZrS_2 monolayer, respectively. A biaxial strain is applied when equal amounts of elongation or compression are imposed on the ZrS_2 monolayer in two perpendicular directions (the x and y planes), while uniaxial strain occurs when elongation or compression is applied in only one direction [46]. We considered a maximum strain of ±5%, as experimental studies have shown that this range preserves the structural integrity of the material [59–61].

Results and discussions

Li adsorption on a ZrS_2 monolayer under zero strain

Understanding the adsorption mechanisms of ions on an electrode is very significant in battery technology. Therefore, we thoroughly investigated the adsorption energies (E_{ads}), adsorption heights (dLi), energy barrier profiles, and electronic properties of a single Li atom on a ZrS_2 monolayer. To achieve this, we identified three typical high-symmetry adsorption sites as shown in Figure 1: (1) H-site Figure 1a, the Li adatom is precisely positioned above the hexagonal center or hollow site; (2) T_1-site Figure 1b, the Li adatom is unambiguously located on the top of an S adatom; and (3) T_2-site Figure 1c, the Li adatom is indisputably situated on the top of a Zr atom.

Where reference [35] reported the values calculated on ZrS_2-graphene heterostructure

The identified sites agree well with previous studies, where they have demonstrated that ZrS_2 monolayer has multiple sites for anchoring adatoms [25, 35]. It is therefore imperative to determine the most energetically stable site through rigorous structural optimization and comprehensive analysis of adsorption energies.

Additionally, to ensure reliable results for adatom adsorption on a ZrS_2 monolayer, it is very important to use a sufficiently large supercell to minimize interactions between periodic images [62], while still adhering to periodic boundary conditions [56]. One effective approach to achieve this is to perform supercell size convergence testing. With that said, supercell sizes were varied as follows: 1×1, 2×2, 3×3, 4×4, and 5×5. Thereafter, a Li atom was adsorbed for each supercell size, and structural optimization was performed to ensure energy minimization.

As mentioned earlier, adsorption energy plays a very critical role in determining the stability and charge/discharge behavior of electrode materials for metal ions. As depicted in Figure 1, the plot demonstrates the consistency of Li adsorption energies (E_{ads}(Li)) at the H-site, T_1-site, and T_2-site across various supercell sizes (1×1, 2×2, 3×3, 4×4, and 5×5) for supercell convergence tests in Figure 2. The adsorption energies at the considered sites exhibit minimal change from the 3×3 supercell size onwards, confirming convergence. Consequently, the 3×3 supercell was selected for further calculations. Moreover, we examined the E_{ads}(Li) on various sites as illustrated in Figure 1 and Table 1: the H-site, T_1-site, and T_2-site on a ZrS_2 monolayer. The negative E_{ads}(Li) values

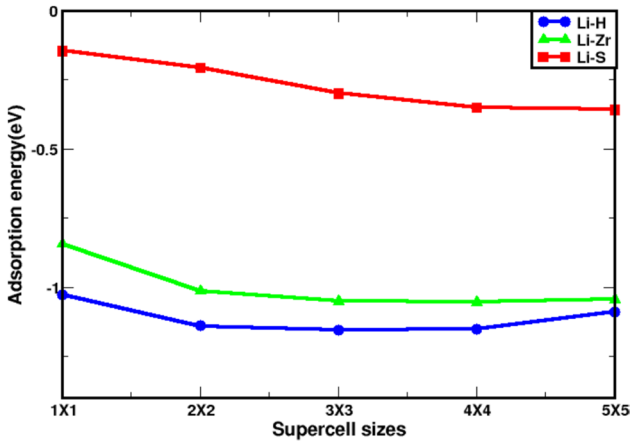

Fig. 2 The influence of supercell size variation on the lithium adsorption energies on a ZrS_2 monolayer

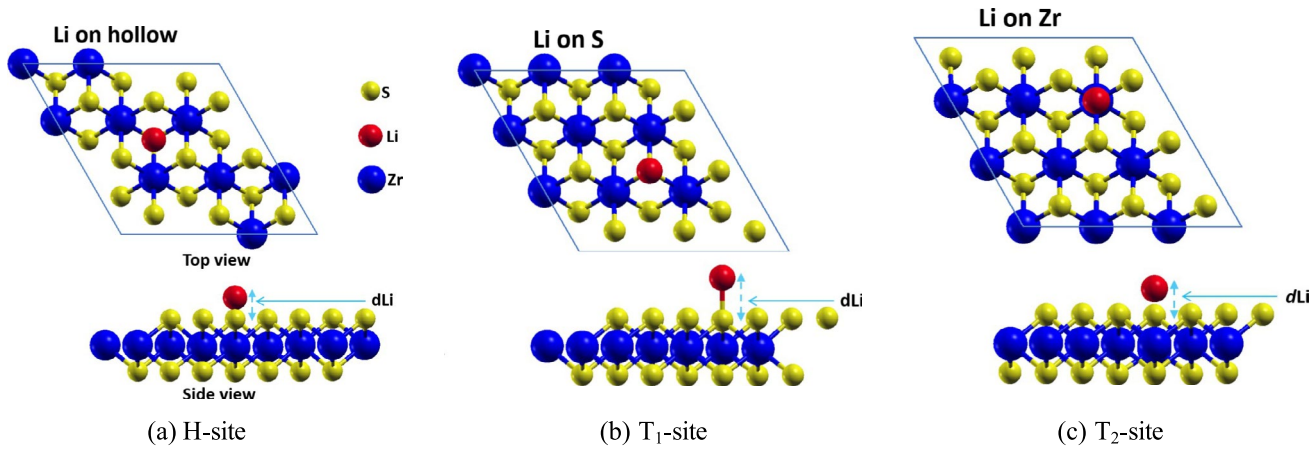

Fig. 1 Optimized ball-and-stick model of the ZrS_2 monolayer. The top diagram shows the top view, while the bottom diagram displays the side view of a ZrS_2 monolayer. Three distinct lithium adsorption sites are illustrated (**a**, **b**, and **c**): corresponding to the H-site, T_1-site, and T_2-site, respectively

Table 1 The calculated adsorption energies E_{ads} (eV) and optimized heights dLi (in Å) for lithium adatoms at different sites (H-site, T_1-site, and T_2-site) of ZrS_2 monolayer

Li sites	E_{ads} (eV)	dLi (Å)
H-site	− 1.16 (− 0.88) [35]	1.21
T_1-site	− 0.30 (0.22) [35]	2.22
T_2-site	− 1.05 (− 0.71) [35]	1.35

for the considered sites indicate an exothermic adsorption process, suggesting significant electronic interaction between the lithium adatoms and the ZrS_2 monolayer. This finding is consistent with previous research on Li adatom interactions with other two-dimensional materials [63–65], affirming the potential of a ZrS_2 monolayer as a suitable cathode material for lithium-ion battery applications. Among the considered adsorption sites, the H-site exhibits the lowest E_{ads}(Li) value of −1.16 eV, obtained from 3 × 3 supercell sizes, indicating its favorability. This observation aligns with the findings of King'ori et al. [35], who investigated the energetic stability of Li in a graphene-ZrS_2 monolayer heterostructure. This suggests a strong interaction between Li-ions and the ZrS_2 monolayer, minimizing the formation of unwanted clusters. The optimized Li height (dLi (Å)) for the considered sites, measured above the outermost sulfur, is detailed in Table 1. The H-site shows the shortest dLi of 1.21 Å, indicating a greater interaction.

Meanwhile, the T_1-site demonstrates the highest E_{ads}(Li) of −0.30 eV and a relatively longer value of 2.2 Å, indicating a weaker interaction. This observation aligns with the findings of Rehman et al. [25], who reported binding energies of Li at different sites as 1.41 eV (H-site) and 1.31 eV (T_2-site) while excluding the T_1-site due to its high energetic instability [25]. The substantial variation in stability among these sites can be attributed to their distinct Li adatom coordination and differing electronegativity. The T_1-site involves single coordination between the Li adatom and the nearest outermost S atom, whereas the H-site entails multiple coordination between Li and the nearest outermost S atoms. Rehman et al. [25] suggested that the higher electronegativity of the S atom compared to the Zr atom results in the acceptance of lithium's valence electrons, leading to a strong ionic bond and greater stability. The smaller difference in adsorption energy between the H-site (−1.16 eV) and the T_2-site (−1.05 eV) could be attributed to the high number of Li adatom co-ordinations with S atoms in both sites. Consequently, their optimized dLi values are also small, as shown in Table 1. The relatively higher stability of the H-site compared to other sites (Figure 2) indicates its preference for Li atom adsorption, potentially enhancing the overall electrochemical performance of the ZrS_2 monolayer. Consequently, subsequent calculations focused on the H-site.

Li adsorption and charge density distribution on ZrS_2 monolayer under uniaxial and biaxial strains

Understanding how strain affects materials is essential, as it will allow us to tailor their properties for specific technological applications. Previous studies have shown that applying strain can alter various properties of two-dimensional materials [18, 19, 59, 66–68], such as enhancing the stability and electrochemical properties, showing great promise for improving material performance. Thus, we investigated the effects of uniaxial and biaxial strains on the energetic stability and structural properties of lithium atom adsorption on the ZrS_2 monolayer. We subjected the ZrS_2 monolayer to both uniaxial (depicted in Figure 3a) and biaxial (depicted in Figure 3b) strains, with a 1.25% increase in tensile and compressive magnitudes ranging from −5% to 5%, as depicted in Figure 3c of adsorption energies. The relaxed structures of single Li adsorption on a 3 × 3 ZrS_2 monolayer under uniaxial (Figure 3a) and biaxial (Figure 3b) strains at −5% and 5% strains remain intact. It was previously reported that this magnitude of strain can be achieved experimentally without deforming the structure [41, 42, 48].

Following the structural optimization, we investigated the effects of strains on the adsorption energy of Li at an H-site of the ZrS_2 monolayer. Figure 3c demonstrates that the calculated adsorption energies are consistently negative, indicating the sustained exothermic nature of the reaction of Li with the ZrS_2 monolayer across the range of applied strains. Moreover, the adsorption energy (E_{ads}) exhibits sensitivity to strain application, as depicted in Figure 3c. Under both uniaxial and biaxial strains, E_{ads} decreased under compressive strain and increased under tensile strain compared to the 0% strain reference, as shown in Figure 3c. Most importantly, under compressive strain, biaxial strain yielded more stable structures (e.g., −1.25% results in E_{ads}=−1.21 eV, −2.5% results in E_{ads}= −1.27 eV, −5% results in E_{ads}= −1.40 eV) compared to uniaxial strain (e.g., −1.25% results in E_{ads}= −1.1 eV, −2.5% results in E_{ads}= −1.23 eV, −5% results in E_{ads}= −1.31 eV). Biaxial strain under compressive force proves advantageous in enhancing the Li-ion ZrS_2 monolayer interactions.

Figure 3d depicts the impact of both uniaxial and biaxial strains on the dLi above the ZrS_2 monolayer. When subjected to compressive strain, biaxial strain notably increased dLi compared to the 0% strain reference (e.g., −1.25% results in dLi= 1.19 Å, −2.5 Å% results in dLi= 1.23 Å, −3.75% yields dLi= 1.24 Å, −5% yields dLi= 1.25 Å). This suggests that biaxial compression reduces the interatomic distances between Zr and S atoms from 2.59 Å to 2.54 Å (Figure 3b), causing their electronic states to overlap slightly, which could lead to the repulsion of the Li-ions. For the case of uniaxial strain (Figure 3d), on the other hand, it does not result in significant variations in dLi values (e.g., −1.25%

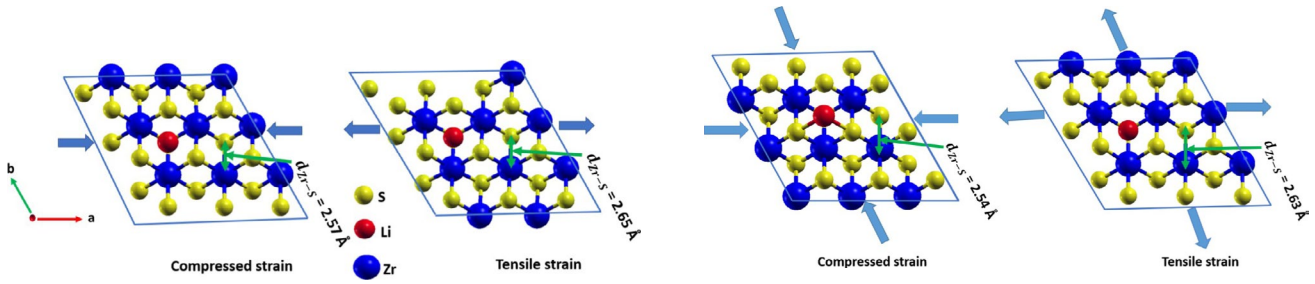

(a) Applied uniaxial strain at -5% and 5%

(b) Applied biaxial strain at -5% and 5%

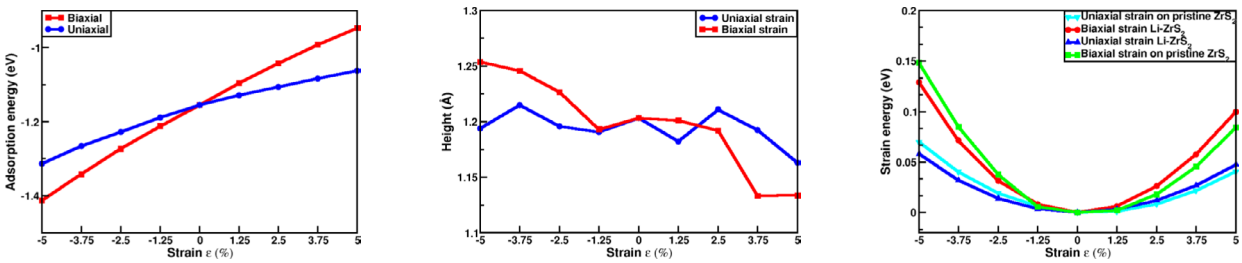

(c) (d) (e)

Fig. 3 The relaxed structures of single Li adsorption on a 3 ×3 ZrS_2 monolayer under **a** uniaxial and **b** biaxial strains, specifically at −5% and 5%. **c** Variation in adsorption energy E_{ads} as a function of uniaxial and biaxial strain percentages applied to Li-ZrS_2 monolayer. Negative strain percentages represent compressive strains, while positive percentages represent tensile strains. **d** Variation in Li height dLi above the ZrS_2 monolayer as a function of uniaxial and biaxial strain percentages. **d** Strain energy ΔE as a function of uniaxial and biaxial strain percentages applied to both the pristine ZrS_2 monolayer and the Li-ZrS_2 monolayer structures

results in dLi= 1.19 Å, −2.5% results in dLi= 1.20 Å, −3.75% yields dLi= 1.22 Å, and −5% yields dLi= 1.19 Å).

When subjected to tensile strain, uniaxial strain results in greater stability (e.g., 1.25% results in E_{ads}= −1.13 eV, 2.5% results in E_{ads}=−1.11 eV, 5% results in E_{ads}= −1.06 eV) compared to biaxial strain (e.g., 1.25% results in E_{ads}= −1.10 eV, 2.5% results in E_{ads}= −1.04 eV, 5% results in E_{ads}= −0.5 eV). Prior research indicates that tensile strain influences the adsorption of Li/Na atoms on two-dimensional materials [40, 48, 49]. In contrast, under both uniaxial and biaxial tensile strains, the dLi decreased. Biaxial strain notably decreases dLi compared to the 0% strain reference (e.g., 1.25% results in dLi= 1.20 Å, 2.5% results in dLi= 1.21 Å, 3.75% results in dLi= 1.13 Å, 5% results in dLi= 1.13 Å), while uniaxial strain does not cause significant variations in dLi values (e.g., 1.25% results in dLi=1.18 Å, 2.5% results in dLi= 1.21 Å, 3.75% results in dLi= 1.19 Å, 5% results in dLi=1.16 Å). Biaxial strain likely elongates the bond lengths between Zr and S atoms from 2.59 to 2.63 Å (Figure 3b), reducing the overlap between their electronic states. This reduction in overlap could lead to an increased attraction for Li-ions.

It is important to assess the energetic stability of strained Li-ZrS_2 monolayer structures through strain energy analyses. The strain energy (ΔE) is determined as the difference in energy between the strained and unstrained structures [19]. Therefore, the following equation is used:

$$\Delta E = E_S - E_U \tag{3}$$

The E_S and E_U terms represent the total energies of strained and unstrained Li-ZrS_2 monolayer structures, respectively.

Figure 3e illustrates the dependence of strain energy on variations in uniaxial and biaxial strain percentages for both pristine and Li-ZrS_2 monolayer structures. All the plots in Figure 3e exhibit a quadratic relation during both compression and tensile strains, indicating that both pristine and Li-ZrS_2 monolayer structures undergo reasonable elastic deformation. This observation is consistent with previous studies [19, 59]. Starting with the analysis of uniaxial and biaxial strains applied to the pristine ZrS_2 monolayer, it is observed that biaxial strain consistently results in higher changes in strain energy (ΔE) compared to uniaxial strain. This is particularly noticeable within the strain ranges of −1.25% to −5% (compressive strain) and +1.25% to +5% (tensile strain). The value of ΔE = 0.15 eV at −5% biaxial strain is consistent with previous studies [59] and is larger than that at +5% strain. This could be attributed to the fact that the repulsive forces between atoms under external compression

to the pristine ZrS_2 monolayer require more energy than the attractive forces between atoms under tensile strain.

For the application of uniaxial and biaxial strains to the Li-ZrS_2 monolayer structure, it is found that the presence of a Li adatom slightly reduces the ΔE in the compressive region (−1.25% to −5%) compared to their pristine counterparts, as shown in Figure 3e. Conversely, the Li adatom slightly increases the ΔE in the tensile region (+1.25% to +5%). Nonetheless, the ΔE values in the compressive region remain marginally higher than those in the tensile region, indicating the predominance of atomic repulsive forces due to compression. The close agreement between the ΔE values of the pristine and Li-ZrS_2 monolayer structures indicates that both have the potential to retain high elasticity before undergoing plastic deformation.

Furthermore, to fully comprehend the electronic interactions between the adsorbed Li and ZrS_2, we investigated the charge density distributions in the systems. Notably, the investigations were done on the zero strain and extremes of −5% and +5% strains. The results revealed that charge density was accumulated (pink) towards the ZrS_2, specifically from the Li to the Zr atoms as shown in Fig. S2. Most interestingly, the accumulation of charge density for all the considered systems at different strains had a similar trend of charge density cloud with the same iso-value of 0.0025 a.u. (Fig. S2). Nonetheless, Bader's analysis revealed slight differences in the quantified charge density transferred; for the zero strain, it was 0.910 |e|; for +5%, it was 0.911 |e|; whereas for −5%, it was found to be 0.908 |e|. These slight differences could be a result of structural change due to external forces. Ultimately, the results showed that there are electronic interactions between the Li and ZrS_2 despite the application of different strains, which is significant for the anode material as it helps to stabilize charging of the ions and transport during the operation of the battery.

Diffusion of Li-ion on strained ZrS_2 monolayer

The mobility of metal ions on an electrode plays a crucial role in determining the efficiency of the battery's charging and discharging processes. It is heavily influenced by the energy barriers present on the electrode surface. To gain insights into how uniaxial and biaxial strains affect the mobility of Li-ions across a ZrS_2 monolayer, we performed calculations of the diffusion energy barriers using the nudged elastic band (NEB) technique [69]. We created a series of visually descriptive images, representing lithium ions as red balls (Figure 4), to illustrate the high-symmetry diffusion paths and estimate the minimal energy path (MEP) that lithium ions follow across the surface of a ZrS_2 monolayer. Figure 4 showcases the ZrS_2 monolayer structures, with two distinct diffusion paths marked by red chained balls. Path 1 involves a lithium-ion starting at an H-site and moving to an adjacent H-site (i.e., H-site to H-site), as depicted in Figure 4a. Path 2 depicts a lithium-ion starting at an H-site, passing through a T_1-site and a T_2-site, and ending at another H-site, as shown in Figure 4b. Figure 4a and b showcase the energy profiles for Path 1 and Path 2 under biaxial strain, respectively, while Figure 4c and d present the energy profiles for Path 1 and Path 2 under uniaxial strain.

After the calculations, energy barriers for the two paths were compared at 0 strain condition; Path 1 (Figure 4a) demonstrated a low energy barrier of 0.22 eV, whereas Path 2 shows a higher energy barrier of 0.86 eV (Figure 4b).

Hence, this suggests that Li-ions favor Path 1 due to its lower energy barrier, enabling efficient movement and ensuring an excellent charge/discharge rate. Our obtained diffusion energy barrier for Path 1 is consistent with previous studies on a variety of 2D materials, such as ZrS_2 (0.24 eV) [25], graphene (0.31 eV) [70], MoS_2 (0.19 eV) [71], and SnS_2 (0.61 eV) [72]. In addition, the impact of strains on Li-ion mobility is depicted by the energy barrier profiles presented in Figure 4a and b for biaxial strain and Figure 4c and d for uniaxial strain.

Delving into Path 1, both uniaxial and biaxial strains marginally decreased the diffusion energy barriers under compression (Figure 4a): When ZrS_2 gets compressed, the S at the saddle point shifts slightly away from the Li, hence decreasing the electronic interaction and subsequently reducing the energy barrier, whereas with tensile strain, the ZrS_2 remained rigid, maintaining the distance between the S at the saddle point and Li (Figure 4b). Hence, the diffusion energy barrier is almost similar to that of an unstrained system. This finding aligns with previous related studies suggesting that Li-ion diffusion in other 2D materials is not significantly impacted by tensile strain application [40, 48]. Ultimately, the application of strains was observed to have a minimal effect on the diffusion energy barriers, unlike its significant influence on the adsorption energies of the Li on ZrS_2. This is important as it shows strain applications to enhance the performance of anode materials in Li-ion batteries.

Effects of biaxial strain on electronic properties of Li-ZrS_2 monolayer

The electronic conductivity of an electrode is a crucial property for battery performance, requiring excellent electronic conductivity in the material. Our study investigated the impact of biaxial strain on the electronic conductivity of Li-ZrS_2 monolayers. By analyzing spin-up and spin-down density of states (DOS) and partial density of states (PDOS) plots in Figure 5, we examined the total and partial DOS contributions of pristine ZrS_2, as well as those of Li-ZrS_2 with and without strain. The spin-up and spin-down DOS plots for pristine ZrS_2 in Figure 5a reveal it as a band

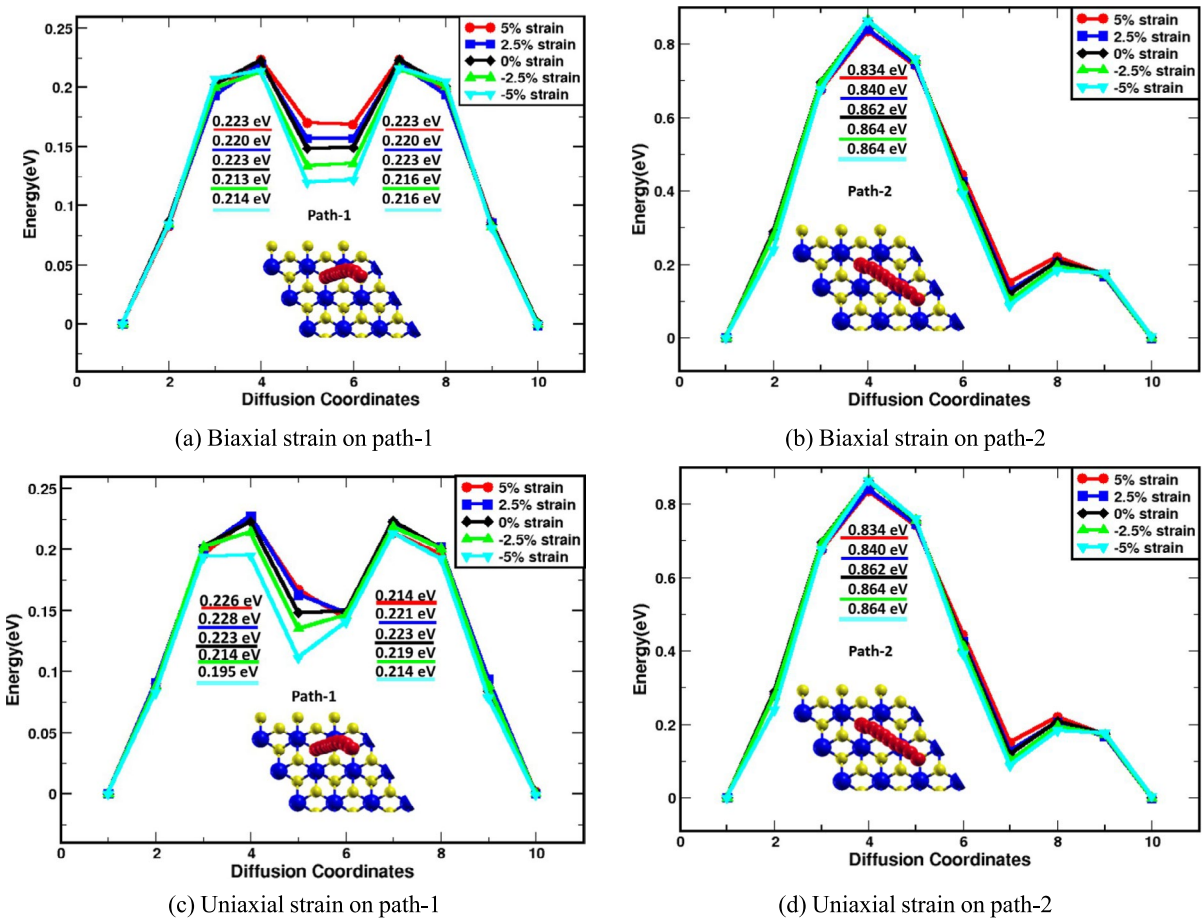

(a) Biaxial strain on path-1

(b) Biaxial strain on path-2

(c) Uniaxial strain on path-1

(d) Uniaxial strain on path-2

Fig. 4 The Li-ion diffusion possible paths and energy barrier profiles at different strains

gap material with poor electrical conductivity, consistent with previous literature [19, 26, 29, 73]. Using the DFT+U approach, we obtained a band gap value of 1.62 eV, in agreement with prior studies [29].

The material's HSE and PBE band gap values range from 1.53 to 1.95 eV and 1.12 to 1.20 eV, respectively, as reported in [19, 26–28]. Experimental studies have firmly established band gap values of 1.68 eV [27], 1.7 eV [28], and 1.78 eV [30]. The PDOS effectively showcases the orbital contributions to the valence band maximum (VBM) and the conduction band minimum (CBM) of the pristine ZrS_2 monolayer, as depicted in Figure 5a. Sulfur p orbitals dominate the VBM states, while the CBM states are greatly contributed to by zirconium d orbitals, with slight hybridization from sulfur p and s orbitals, as demonstrated in previous studies [73].

Figure 5b illustrates the DOS and PDOS for the Li-ZrS_2 structure. It is important to highlight that the introduction of Li on ZrS_2 monolayer resulted in the spin-down states crossing the Fermi level [25] closer to the CBM. The conductive states induced are mainly attributed to the hybridization of the Zr d orbitals (Figure 5b), indicating that Li adsorption has a significant impact on the CBM of the ZrS_2 monolayer. According to Hammer et al., the d states/bands for surfaces play a crucial role in the reactivity with metal atoms [74, 75]. The states associated with the Li become relatively flat near the Fermi level. The band gap magnitude has increased from 1.62 to 1.82 eV due to the rearrangement of Zr d states responsible for the CBM. Additionally, the introduction of Li caused the Fermi level to shift closer to the CBM edge, indicating the transfer of extra electrons into the ZrS_2 monolayer system. When subjected to a 2.5% tensile strain, the Li-ZrS_2 supercell demonstrates a widening of the band gap from 1.82 to 2.41 eV, as depicted in Figure 5c. This strain causes a shift of the Fermi level away from the conduction band minimum (CBM) towards the in-gap region. Additionally, the resulting d states exhibit a flatter profile as they intersect the Fermi level, suggesting a decrease in conductivity due to the tensile strain. Conversely, a compressive strain of −2.5% leads to a reduction of the band gap from 1.82 to 1.68 eV, as shown in Figure 5d. Application of a 5% tensile strain notably increased the band gap to 2.57 eV (Figure 5e), consistent with previous studies [18, 19, 59, 66–68]. Furthermore, a −5% strain (Figure 5f) reduced the band gap to 1.24 eV. These compressive strains notably shift

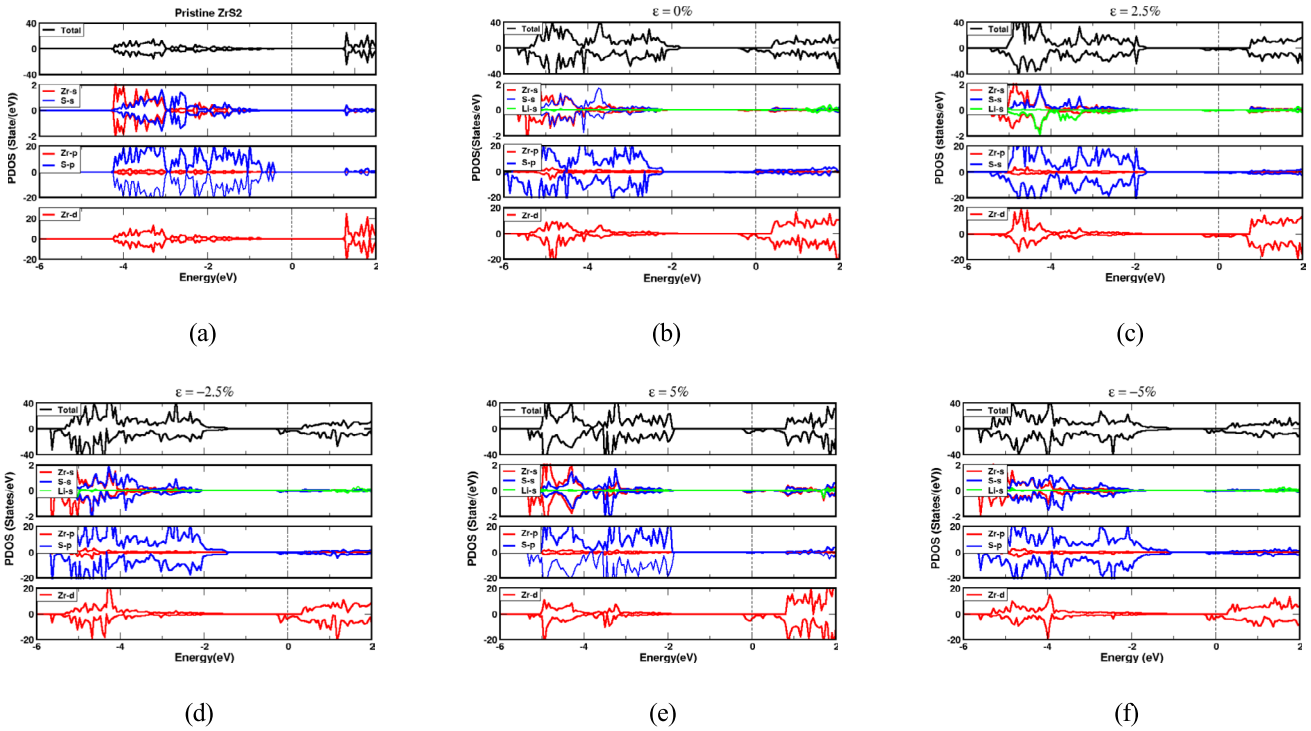

Fig. 5 Total and partial density of states of **a** a pristine ZrS_2 monolayer and **b** Li-ZrS_2 monolayer structures without strain application. The effect of biaxial strain on the density of states of the Li-ZrS_2 monolayer under various strain percentages: **c** 2.5%, **d** − 2.5%, **e** 5%, and **f** − 5%. The Fermi level is set to 0 eV and represented by the black dotted line

the Fermi level closer to the CBM. Additionally, the Zr d orbital states exhibit sharp peaks crossing the Fermi level, indicating enhanced electrical conductivity compared to the tensile strain case.

Effects of biaxial strain on the average adsorption energies, open circuit voltages, and electronic properties of ZrS_2 monolayer adsorbed with multiples of Li-ions

The efficiency of energy utilization is heavily dependent on the adsorption energy, open circuit voltage, and metallic characteristics of an electrode. Our comprehensive analysis of these properties in the ZrS_2 monolayer as a lithium anode began with the calculation of average adsorption energies for multiples of adsorbed Li (1, 2, 4, 6, 8, and 16) corresponding to Li concentrations (x = 0.04, 0.07,0.15, 0.22, 0.30, and 0.60), as depicted in Figure 6. The results revealed a linear increase in adsorption energy (Figure 6a) as the Li increased concentrations from 0.04 to 0.3, indicating a decrease in binding strength with the ZrS_2 monolayer. This trend aligns with findings from a previous related study [25]. The rise in Coulomb repulsive force between the Li-ions with the addition of more Li to one side of the ZrS_2 monolayer is

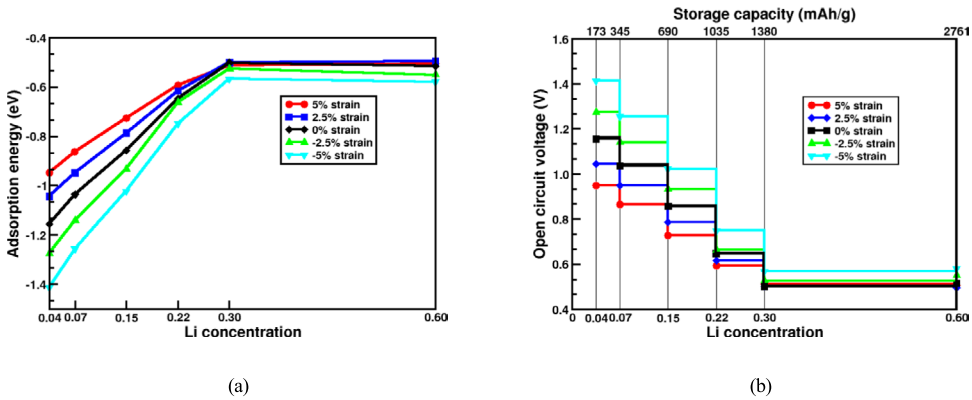

Fig. 6 The calculated average adsorption energies and open circuit voltage at different strains: **a** average adsorption energy and **b** open circuit voltage

believed to be the cause of this effect. Interestingly, when the number of Li exceeded 0.3 and both surfaces were considered, the change in adsorption energy became minimal, resulting in a horizontal plot. This suggests that the ZrS_2 monolayer would require a higher concentration of Li for the adsorption energy to reach 0.00 eV (Bulk Li formation above the ZrS_2 monolayer), hinting at the potential for high Li-specific capacitance.

After subjecting the material to a biaxial strain, we closely observed its impact on adsorption energies. When the strain was increased to 2.5%, the calculated adsorption energies for varying numbers of Li consistently rose in comparison to those at 0% strain. However, these values approached the 0% strain levels when the Li concentration reached 0.3, as illustrated in Figure 6a. A similar trend is observed for a tensile strain of 5%, with higher adsorption energy values indicating a slight reduction in the interaction between Li-ions and the ZrS_2 monolayer. Conversely, under a compressive strain of −2.5%, the adsorption energies for various Li are consistently lower than those at 0% strain (Figure 6a). With a further increase in compressive strain to −5%, the adsorption energies decrease even more, indicating slightly improved binding between Li-ions and the ZrS_2 monolayer. We also calculate the specific capacity C_{Li} of a ZrS_2 monolayer to evaluate the number of lithium ions that an anode can accommodate per unit mass.

This was achieved using the following formula:

$$C_{\mathrm{Li}} = \frac{nZF}{M_{ZrS_2}} \tag{4}$$

where the Faraday constant F is set to 26,801 mAh/mol and M_{ZrS2} is the total molar mass (g/mol) of a $3 \times 3 \times 1$ ZrS_2 monolayer. Z represents the number of valence electrons of Li-ions.

The graph in Figure 7b demonstrates a significant increase in storage capacity with the rise in the Li concentration. Specifically, the storage capacity rises from 173 to 2761 mAh/g as the concentrations increase from 0.04 to 0.60. This impressive storage capacity is anticipated to continue increasing with the Li concentration until amorphization or dendrite formation occurs. It is noteworthy that even at this capacity, the structural integrity of the ZrS_2 monolayer remains intact, underscoring its resilience to lithium adsorption. Our findings of 350 mAh/g (for 0.07 Li concentration) and 700 mAh/g (for 0.15 Li concentration) are in line with the values of 345 mAh/g (for 0.07 Li concentration) and 690 mAh/g (for 0.15 Li concentration) reported by Rehman et al. [25].

Open circuit voltage (OCV) serves as a crucial parameter for evaluating the performance of lithium-ion batteries. Recent research suggests that an ideal anode material should demonstrate a low average OCV to be suitable for rechargeable LIBs [25, 35, 48, 72, 76–78]. It has been observed that OCV values tend to approach zero as the material reaches its maximum lithium-ion insertion capacity. Throughout the charge/discharge cycle of LIBs, the well-known half-cell reversible reaction at the anode ZrS_2 monolayer can be expressed as:

$$Li^+ + ne^- + ZrS_2 \iff Li_nZrS_2 \tag{5}$$

n represents the number of lithium atoms, and e denotes the electronic charge, respectively. The electrons produced in this reaction travel through the battery's external circuit,

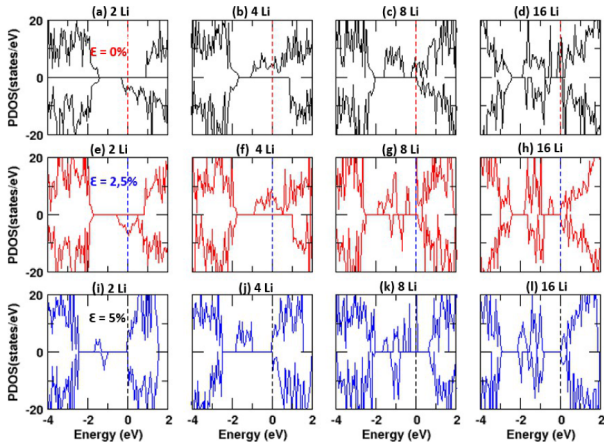

(a)

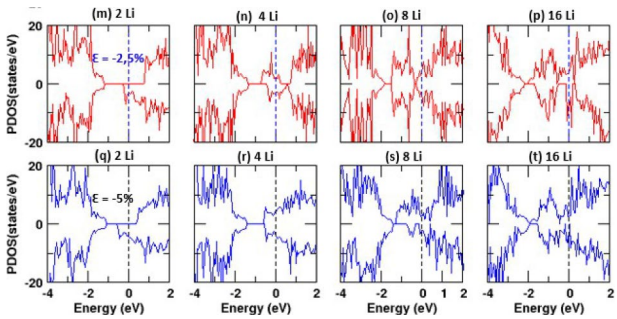

(b)

Fig. 7 (a–d) Total density of states for multiple Li adatoms on a ZrS_2 monolayer without applied strain. The effect of biaxial strain on the density of states of Li adatoms on the ZrS_2 monolayer is examined at various strain percentages: (e–h) 2.5%, (i–l) 5%, (m–p) −2.5%, and (q–t) −5%. The Fermi level is set to 0 eV, indicated by the black dotted line

while positive ions move between the electrodes via the electrolyte.

The OCV is calculated using the following equation:

$$V = -\left(\frac{E_{ZrS_2+ad} - E_{ZrS_2} - nE_{Li}}{ne}\right) \quad (6)$$

Here, E_{ZrS2}+ad represents the total energy of Li adatom at the hollow site of a ZrS_2 monolayer, E_{ZrS2} denotes the total energy of the pristine ZrS_2 monolayer, and E_{ad} refers to the total energy of lithium ions in a bulk BCC structure, respectively.

Figure 7b displays plots of OCV as a function of the Li concentration (0.04, 0.07, 0.14, 0.22, 0.30, and 0.60) under different applied strains ($\varepsilon = -2.5\%$, -5%, 0%, 2.5%, and 5%). The positive OCV values (Figure 7b) indicate that lithium ions have a potential binding with the ZrS_2 monolayer. At zero strain ($\varepsilon = 0\%$), OCV decreases from 1.16 to 0.52 V as the Li concentrations increase from 1 to 0.60. A noted steady constant OCV plot when Li concentrations increase from 0.30 to 0.6 indicates the potential to incorporate the majority of them into a ZrS_2 monolayer supercell. This suggests that additional Li concentrations can still be incorporated beyond 0.60 before the OCV reaches 0.00 V, and beyond this point, metal clusters may begin to form [79]. The average OCV of 0.78 V was calculated by averaging the potential values (V = 1.155, 1.038, 0.644, 0.853, 0.502, and 0.512), which correspond to increasing lithium concentrations as illustrated in Figure 7b at zero strain (ε = 0%). Previous studies report similar OCV values for various monolayers: For example, Rehman et al. [25] found an OCV of 0.7 V for a ZrS_2 monolayer, Bekeur et al. [72] reported 1.34 V for a SnS_2 monolayer, and Hao et al. [48] measured an OCV of 0.65 V for a MoS_2 monolayer. An experimental study of Li deposition on a ZrS_2 monolayer indicates that the acceptable average OCV values should range from 0.1 to 3.00 V [37], which supports our OCV findings. Moreover, it has been reported that as the concentration increases and the discharge voltage approaches 0.1 V, the structure amorphizes into LiS and Zr compounds due to the rise of strong Li repulsive forces [37]. When charged to 0.4 V, the structure reverts to the ZrS_2 crystal form.

We furthermore looked at the influence of the tensile (ε = 2.5% and 5%) and compressive ($\varepsilon = -2.5\%$ and -5%) strains on the OCV (Figure 7b). It is observed that tensile strains of 2.5% and 5% consistently yielded lower OCV values compared to the unstrained condition (0%). As the Li concentration increased from 0.04 to 0.22 above a ZrS_2 monolayer, the OCV values remained lower, but they began to approach those of the unstrained condition when the Li concentration reached 0.30 to 0.60. The resulting average OCV values for 2.5% and 5% strains were calculated to be 0.72 V and 0.69 V, respectively, by averaging the potential values for 2.5% strain (V =1.043, 0.943, 0.740, 0.616, 0.502, and 0.490) and for 5% strain (V = 0.947, 0.863, 0.727, 0.593, 0.512, and 0.506). These values are relatively close to the average OCV under unstrained conditions. For both the -2.5% and -5% compressive strains, the OCV remains above that of the unstrained condition as the Li concentration increased from 0.04 to 0.60 on the ZrS_2 monolayer (see Fig. 5b). This indicates that the ZrS_2 monolayer under -5% strain can accommodate more Li than at 0% strain before the OCV reaches zero. The average OCV values for -2.5% and -5% strains were calculated to be 0.85 V and 0.93 V, respectively, by averaging the potential values for -2.5% strain (V = 1.273, 1.140, 0.932, 0.662, 0.527, and 0.550) and for -5% strain (V = 1.413, 1.255, 1.022, 0.749, 0.567, and 0.580). These values were also found to be higher than the average OCV under the unstrained condition. Thus, we suggest that applying tensile strain on a ZrS_2 monolayer can help mitigate dendrite formation during the battery operations.

Additionally, we analyzed the impact of varying the number of Li-ions on a ZrS_2 monolayer on the DOS. This comprehensive analysis initially was conducted without the application of strain, as illustrated in Figure 7 (a to d), and was subsequently followed by an in-depth investigation under both tensile strain (Figure 7 (e to l)) and compressive strain (Figure 7 (m to t)). Upon the adsorption of two Li atoms, the induced spin-down DOS increased (Figure 7a) as compared to the DOS of a single Li atom, as depicted in Figure 5d. Conversely, with four Li atoms adsorbed on the ZrS_2 monolayer, the induced states shifted to a spin-up orientation, spanning a significant portion of the energy band gap, as shown in Figure 7b. Notably, the induced DOS for four Li atoms exhibited a substantially greater magnitude compared to those for two Li atoms. When eight Li atoms are adsorbed on a ZrS_2 monolayer (Figure 7 (c)), the induced DOS remains predominantly spin-up oriented and spans a large region of the energy band gap. For 16 Li atoms adsorbed on a ZrS_2 monolayer, the induced DOS (Figure 7c) exhibits both spin-up and spin-down orientations spanning within the energy band gap. These induced DOS for 16 Li atoms exhibit a greater magnitude compared to those for a smaller number of Li atoms. The Fermi level for this structure had shifted into the CBM, indicating an increased number of electron transfers due to the adsorption of Li adatoms. Similar behavior was noted in [25]. The observed increase in electrical conductivity of the ZrS_2 monolayer due to Li adsorption is a key property for improving LIBs in terms of the charge and discharge rates. The application of tensile strain on the systems of multiple Li adatoms adsorbed on a ZrS_2 monolayer caused an interesting shift of the induced states from the CBM to the VBM, as shown in Figure 7 (e to h) for 2.5% and Figure 7 (i to l) for 5%. This shift is accompanied by an increase in the band gap, leading to the induced states being separated by small energy gaps.

However, a drawback is that the flow of electronic charges will not be continuous during LIB operation under tensile strain. On the other hand, the application of compressive strain to multiple Li adatoms on a ZrS_2 monolayer reduces the band gap, causing both the induced spin-up and spin-down states to shift from the CBM to the VBM, as illustrated in Figure 7 (m to p) for −2.5% and Figure 7 (q to t) for −5%. Similar behavior is noted for Li on a MoS_2 monolayer [48].

Notably, as the Li concentration increased, the induced states became continuous and the band gap closed, which is also linked to the stability in adsorption observed when the OCV reduced with an increase in Li concentration (Figure 7b). This suggests enhanced conductivity, as the induced DOS reveals that the flow of electronic charges will be continuous during LIB operation under compressive strain.

Conclusions

In summary, DFT was used to investigate the interactions of Li-ions with a ZrS_2 monolayer under uniaxial and biaxial strains. Our results revealed that after a single Li adsorption, the Li-ZrS_2 structures became more energetically favorable as compressive strain increased and less favorable as tensile strain increased, while maintaining an exothermic reaction. The Zr-S bond lengths decreased under compressive strain, causing repulsion of host electronic states and resulting in an increased adsorption height of the Li adatoms. Conversely, tensile strain led to the opposite effect, where Zr-S bond lengths increased and Li adsorption height decreased. Additionally, it was found that the Li adatom prefers to diffuse along Path 1 with an energy barrier of 0.22 eV. By looking at energy barriers for different strains, the general application of strains had a minimal impact on Li-ion diffusion. Furthermore, the analysis of the DOS revealed a transition from semiconductor to metallic behavior, as the spin-down Zr d orbital states crossed the Fermi level near the CBM. Under compressive strain, the induced states became steep, resulting in increased conductivity, whereas under tensile strain, the states became flat, leading to decreased conductivity compared to the unstrained condition. We also investigated the adsorption of multiple Li-ions (up to 16) on the ZrS_2 monolayer under various strains ranging from −5 to +5%. Interestingly, the application of strains had minimal impact on the adsorption energies, particularly between 8 and 16 Li-ions, with only a slight reduction under compressive strain. When 16 Li were adsorbed, an impressive storage capacity of 2761 mAh/g was achieved, corresponding to an OCV of 0.53 V. This finding suggests that more Li concentrations can be adsorbed to reach 0.00 V. Under−5% strain, the average OCV increased to 0.93 V from the unstrained value of 0.78 V, while +5% strain yielded an OCV of 0.69 V. Although both values fall within the acceptable range of 0.1 to 3 V, the tensile strain can be more effective in mitigating the formation of dendrites. Moreover, as the number of Li adatoms on the ZrS_2 monolayer increased, the population of induced spin-up and spin-down states within the band gap also increased. Furthermore, compressive strain reduced the band gap, causing the induced electronic states to be continuous from the VBM to the CBM edges, thereby enhancing the electronic conductivity of the material.

Despite the exceptional results of the ZrS_2 monolayer as an anode material, practical applications require it to be supported, and this aspect has not yet been explored. Therefore, further research is recommended to determine how its electronic and structural properties can be influenced when the ZrS_2 monolayer is supported, especially with low-energy bulk materials such as transition metals, including commonly used electrolytes such as dimethyl carbonate (DMC) and ethyl methyl carbonate (EMC). This approach could be similar to past studies that examined the effect of solvated graphene+ and M_2C_7 monolayers on Na adsorption energies [80]. Additionally, since all the properties in this study were calculated based on the ground state (0 K) DFT approach, we recommend future studies consider the investigation of temperature variation effects on the reported properties, including battery operational temperature of 300 K. This can be achieved using ab initio molecular dynamics (AIMD).

Supplementary Information The online version contains supplementary material available at https://doi.org/10.1007/s10008-025-06365-3.

Acknowledgements The University of Pretoria is acknowledged for its financial and resource support. Many thanks are devoted to the CHPC platform for providing us with the extensive computational resources. The National Institute for Theoretical and Computational Sciences (NITheCS) and the National Research Foundation (NRF) of South Africa are acknowledged for their financial support.

Funding Open access funding provided by University of Pretoria.

Declarations

Conflict of interest The authors declare no competing interests.

Open Access This article is licensed under a Creative Commons Attribution 4.0 International License, which permits use, sharing, adaptation, distribution and reproduction in any medium or format, as long as you give appropriate credit to the original author(s) and the source, provide a link to the Creative Commons licence, and indicate if changes were made. The images or other third party material in this article are included in the article's Creative Commons licence, unless indicated otherwise in a credit line to the material. If material is not included in the article's Creative Commons licence and your intended use is not permitted by statutory regulation or exceeds the permitted use, you will need to obtain permission directly from the copyright holder. To view a copy of this licence, visit http://creativecommons.org/licenses/by/4.0/.

References

1. Li M, Lu J, Chen Z, Amine K (2018) 30 years of lithium-ion batteries. Adv Mater 30(33):1800561
2. Dahn JR, Zheng T, Liu Y, Xue JS (1995) Mechanisms for lithium insertion in carbonaceous materials. Science 270(5236):590–593
3. Liu J, Liu C, Ye X, Yan X (2018) Monolayer InP_3 as a reversible anode material for ultrafast charging lithium- and sodium-ion batteries: a theoretical study. J Mater Chem A 6(8):3634–3641
4. Xu J, Wang D, Lian R, Gao X, Liu Y, Yury G, Chen G, Wei Y (2019) Structural prediction and multilayer Li+ storage in two-dimensional VC_2 carbide studied by first-principles calculations. J Mater Chem A 7(15):8873–8881
5. Tarascon JM, Armand M (2001) Issues and challenges facing rechargeable lithium batteries. Nature 414(6861):359–367
6. Dunn B, Kamath H, Tarascon J (2011) Electrical energy storage for the grid: a battery of choices. Science 334(6058):928–935
7. Daniel C, Besenhard J O (2012) Handbook of battery materials. John Wiley & Sons. https://doi.org/10.1002/9783527637188
8. Zhang W, Liu Y, Guo Z (2019) Approaching high-performance potassium-ion batteries via advanced design strategies and engineering. Sci Adv 5(5):7412
9. Pistoia G (1993) Lithium batteries: new materials, developments and perspectives, vol 5. Elsevier
10. Rojaee R, Shahbazian-Yassar R (2020) Two-dimensional materials to address the lithium battery challenges. ACS Nano 14(3):2628–2658
11. Zhang C, Jiao Y, He T, Ma F, Kou L, Liao T, Bottle S, Du A (2017) Two-dimensional GeP_3 as a high-capacity electrode material for Li-ion batteries. Phys Chem Chem Phys 19(38):25886–25890
12. Akash A, Singla G, Hameed T, Jha P K (2024) A mini review on two-dimensional (2D) materials for energy storage applications. E3S Web of Conferences 509:3004. https://doi.org/10.1051/e3sconf/202450903004
13. Zhu J, Xiao G, Zuo X (2020) Two-dimensional black phosphorus: an emerging anode material for lithium-ion batteries. Nano-Micro Letters 12:1–25
14. Ali HG, Khan K, Hanif M B, Khan M Z, Hussain I, Javed M S, AL-bonsrulah H AZ, Mosiałek M, Fichtner M, Motola M (2023) Advancements in two-dimensional materials as anodes for lithium-ion batteries: exploring composition-structure-property relationships, emerging trends, and future perspectives. J Energy Storage 73:108980. https://doi.org/10.1016/j.est.2023.108980
15. Wong H, Li Y, Wang J, Tang T, Cai Y, Xu M, Li H, Kim T, Luo Z (2023) Two-dimensional materials for high-density, safe, and robust metal anode batteries. Nano Convergence 10(1):37
16. Xiao Z, Wang R, Jiang D, Qian Z, Li Y, Yang K, Sun Y, Zeng Z, Wu F (2021) Recent developments of two-dimensional anode materials and their composites in lithium-ion batteries. ACS Appl Energy Mater 4(8):7440–7461
17. Ataca C, Sahin H, Ciraci S (2012) Stable, single-layer MX_2 transition-metal oxides and dichalcogenides in a honeycomb-like structure. J Phys Chem C 116(16):8983–8999
18. Xu C, Brown PA, Shuford KL (2015) Strain-induced semimetal-to-semiconductor transition and indirect-to-direct band gap transition in monolayer 1 T – TiS_2. RSC Adv 5(102):83876–83879
19. Zhang J, Gao X, Wei X, Huang Y, Ali A, Shahid I (2022) Tailoring the electronic and optical properties of ZrS_2/$ZrSe_2$ vdW heterostructure by strain engineering. Thin Solid Films 755:139332
20. Jang J, Jeong S, Seo J, Kim M, Sim E, Oh Y, Nam S, Park B, Cheon J (2011) Ultrathin zirconium disulfide nanodiscs. J Am Chem Soc 133(20):7636–7639
21. Zhang M, Zhu Y, Wang X, Feng Q, Qiao S, Wen W, Chen Y, Cui M, Zhang J, Cai C et al (2015) Controlled synthesis of ZrS_2 monolayer and a few layers on hexagonal boron nitride. J Am Chem Soc 137(22):7051–7054
22. Li L, Fang X, Zhai T, Liao M, Gautam UK, Wu X, Koide Y, Bando Y, Golberg D (2010) Electrical transport and high-performance photoconductivity in individual ZrS (2) nanobelts. Adv Mater (Deerfield Beach, Fla.) 22(37):4151–4156
23. Wang X, Huang L, Jiang X, Li Y, Wei Z, Li J (2016) Large-scale ZrS_2 atomically thin layers. J Mater Chem C 4(15):3143–3148
24. Zhang X, Meng Z, Rao D, Wang Y, Shi Q, Liu Y, Wu H, Deng K, Liu H, Lu R (2016) Efficient band structure tuning, charge separation, and visible-light response in ZrS_2-based van der Waals heterostructures. Energy Environ Sci 9(3):841–849
25. Rehman S, Samad A, Saeed M, Amin B, Hafeez M, Mir IA et al (2021) Computational insight of ZrS2/graphene heterobilayer as an efficient anode material. Appl Surf Sci 551:149304
26. Li Y, Kang J, Li J (2014) Indirect-to-direct band gap transition of the ZrS_2 monolayer by strain: first-principles calculations. RSC Adv 4(15):7396–7401
27. Greenaway DL, Nitsche R (1965) Preparation and optical properties of group IV–VI2 chalcogenides having the CdI_2 structure. J Phys Chem Solids 26(9):1445–1458
28. Moustafa M, Zandt T, Janowitz C, Manzke R (2009) Growth and band gap determination of the ZrSx Se2-x single crystal series. Phys Rev B—Condensed Matter Mater Phys 80(3):035206
29. Kumar A, He H, Pandey R, Ahluwalia PK, Tankeshwar K (2015) Semiconductor-to-metal phase transition in monolayer ZrS_2: GGA+ U study. AIP Conference Proceedings 1665(1):090016. https://doi.org/10.1063/1.4917996
30. Roubi L, Carlone C (1988) Resonance Raman spectrum of HfS_2 and ZrS_2. Phys Rev B 37(12):6808
31. Si Y, Wu H, Yang H, Huang W, Yang K, Peng P, Huang G (2016) Dramatically enhanced visible light response of monolayer ZrS_2 via non-covalent modification by double-ring tubular B 20 cluster. Nanoscale Res Lett 11:1–7
32. Lu Y, Zhang Q, Chen J (2019) Recent progress on lithium-ion batteries with high electrochemical performance. Sci China Chem 62:533–548
33. Whittingham MS (1976) Electrical energy storage and intercalation chemistry. Science 192(4244):1126–1127
34. Cheng F, Liang J, Tao Z, Chen J (2011) Functional materials for rechargeable batteries. Adv Mater 23(15):1695–1715
35. King'ori GW, Ouma CNM, Amolo GO, Makau NW (2021) Ab initio insights into Graphene-Zirconium disulfide/diselenide heterostructure as electrode material for alkali-ion batteries. Surfaces and Interfaces 24:101036
36. Ahmad N, Klipstein PC, Obertelli SD, Marseglia EA, Friend RH (1987) Metallic properties of lithium-intercalated ZrS_2. J Phys C: Solid State Phys 20(26):4105
37. Kim S, Kim YJ, Ryu W (2021) Zirconium disulfides as an electrode material alternative for Li-ion batteries. Appl Surf Sci 547:149029
38. Kripalani DR, Kistanov AA, Cai Y, Xue M, Zhou K (2018) Strain engineering of antimonene by a first-principles study: mechanical and electronic properties. Phys Rev B 98(8):085410
39. Carrascoso F, Li H, Frisend R, Castellanos-Gomez A (2021) Strain engineering in single-, bi-and tri-layer MoS_2, $MoSe_2$, WS_2 and WSe_2. Nano Res 14:1698–1703
40. Chen HJ, Huang J, Lei XL, Wu MS, Liu G, Ouyang CY, Xu B (2013) Adsorption and diffusion of lithium on MoS_2 monolayer: the role of strain and concentration. Int J Electrochem Sci 8(2):2196–2203
41. Bertolazzi S, Brivio J, Kis A (2011) Stretching and breaking of ultrathin MoS_2. ACS Nano 5(12):9703–9709

42. Castellanos-Gomez A, Poot M, Steele G A, Van Der Zant H S J, Agraït N, Rubio-Bollinger G (2012) Elastic properties of freely suspended MoS_2 nanosheets. https://doi.org/10.1002/adma.201103965
43. Conley HJ, Wang B, Ziegler JI, Haglund RF Jr, Pantelides ST, Bolotin KI (2013) Bandgap engineering of strained monolayer and bilayer MoS_2. Nano Lett 13(8):3626–3630
44. Hui YY, Liu X, Jie W et al (2013) Exceptional tunability of band energy in a compressively strained trilayer MoS_2 sheet. ACS Nano 7(8):7126–7131
45. Castellanos-Gomez A, Roldán R, Cappelluti E et al (2013) Local strain engineering in atomically thin MoS_2. Nano Lett 13(11):5361–5366
46. Guo H, Lu N, Wang L, Wu X, Zeng XC (2014) Tuning electronic and magnetic properties of early transition-metal dichalcogenides via tensile strain. J Phys Chem C 118(13):7242–7249
47. Song Q, Liu X, Wang H, Wang X, Ni Y, Wang H (2021) Strain-tuned structural, mechanical and electronic properties of two-dimensional transition metal sulfides ZrS_2: a first principles study
48. Hao J, Zheng J, Ling F, Chen Y, Jing H, Zhou T, Fang L, Zhou M (2018) Strain-engineered two-dimensional MoS_2 as anode material for performance enhancement of Li/Na-ion batteries. Sci Rep 8(1):2079
49. Wang H, Luo W, Wu M, Ouyang C (2020) The effect of strain on the Li-storage performance of V_2C and Nb_2C: from first-principles study. Solid State Commun 311:113857
50. Capelle K (2006) A bird's-eye view of density-functional theory. Braz J Phys 36:1318–1343
51. Giannozzi P, Baroni S, Bonini N, Calandra M, Car R, Cavazzoni C, Ceresoli D, Chiarotti GL, Cococcioni M, Dabo I et al (2009) QUANTUM ESPRESSO: a modular and open-source software project for quantum simulations of materials. J Phys: Condens Matter 21(39):395502
52. Perdew JP, Burke K, Ernzerhof M (1996) Generalized gradient approximation made simple. Phys Rev Lett 77(18):3865
53. Monkhorst HJ, Pack JD (1976) Special points for Brillouin-zone integrations. Phys Rev B 13(12):5188
54. Blöchl PE (1994) Projector augmented-wave method. Phys Rev B 50(24):17953
55. Methfessel MPAT, Paxton AT (1989) High-precision sampling for Brillouin-zone integration in metals. Phys Rev B 40(6):3616
56. Kittel C, McEuen P (2018).Introduction to solid state physics, 9th edn. Wiley
57. Grimme S, Antony J, Ehrlich S, Krieg H (2010) A consistent and accurate ab initio parametrization of density functional dispersion correction (DFT-D) for the 94 elements H-Pu. J Chem Phys 132(15). https://doi.org/10.1063/1.3382344
58. Jónsson H, Mills G, Jacobsen KW (1998) Nudged elastic band method for finding minimum energy paths of transitions. Classical and quantum dynamics in condensed phase simulation: 385–404. https://doi.org/10.1142/9789812839664_0016
59. Zhang Y, Duan L, Fan J, Ni L (2022) Effects of the in-plane uniaxial and biaxial strains on the structural and electronic properties of the monolayer ZrS_2: a first-principles investigation. Thin Solid Films 755:139343
60. Lv HY, Lu WJ, Shao DF, Lu HY, Sun YP (2016) Strain-induced enhancement in the thermoelectric performance of a ZrS_2 monolayer. J Mater Chem C 4(20):4538–4545
61. Yuan J, Yu N, Wang J, Xue K, Miao X (2018) Design lateral heterostructure of monolayer ZrS_2 and HfS_2 from first principles calculations. Appl Surf Sci 436:919–926
62. Freysoldt C, Grabowski B, Hickel T, Neugebauer J, Kresse G, Janotti A, Van de Walle CG (2014) First-principles calculations for point defects in solids. Rev Mod Phys 86(1):253–305
63. Sahoo S, Kumari P, Som NN, Kar S, Ahuja R, Ray SJ (2024) Remarkable enhancement of the adsorption and diffusion performance of alkali ions in two-dimensional (2D) transition metal oxide monolayers via Ru-doping. Sci Rep 14(1):4371
64. Zhou L, Hou ZF, Wu L (2012) First-principles study of lithium adsorption and diffusion on graphene with point defects. J Phys Chem C 116(41):21780–21787
65. Mapasha RE, Chetty N (2010) Ab initio studies of staggered Li adatoms on graphene. Comput Mater Sci 49(4):787–791
66. Yang L, Cui X, Zhang J, Wang K, Shen M, Zeng S, Dayeh SA, Feng L, Xiang B (2014) Lattice strain effects on the optical properties of MoS_2 nanosheets. Sci Rep 4(1):5649
67. Tan S, Li R, Yuan H, Chen L, Zeng J, Jiang T (2024) Adsorption and gas sensing properties of Pdn (n=1–3) cluster-modified $PtSe_2$ on transformer fault characterizing gases under biaxial strain and electric field. Colloids and Surfaces A: Physicochemical and Engineering Aspects :134500. https://doi.org/10.1016/j.colsurfa.2024.134500
68. Bao J, Liu G, Yang L, Li F, Yang Z, Zhang G (2024) Exploring electronic features in monolayer and bilayer MX_2 (M= Hf, Zr; X= S, Se) structures under shear strain. Mater Today Commun 39:108962
69. Henkelman G, Uberuaga BP, Jónsson H (2000) A climbing image nudged elastic band method for finding saddle points and minimum energy paths. J Chem Phys 113(22):9901–9904
70. Hao F, Chen X (2015) First-principles study of lithium adsorption and diffusion on graphene: the effects of strain. Mater Res Express 2(10):105016
71. Ersan F, Gokoglu G, Akturk E (2015) Adsorption and diffusion of lithium on monolayer transition metal dichalcogenides (MoS_2 (1–x) Se2x) alloys. J Phys Chem C 119(52):28648–28653
72. Bekeur CA, Mapasha RE (2023) Enhancement of electrochemical performance of monolayer SnS_2 for Li/Na-ion batteries through a sulphur vacancy: a DFT study. J Solid State Electrochem 27(9):2445–2456
73. Abutalib MM (2019) A DFT-based prediction of a new 2D zirconium disulfide Pmmm-ZrS_2 monolayer: a quasi-direct band gap semiconductor. Results Phys 12:903–907
74. Hammer BJKN, Nørskov JK (1995) Electronic factors determining the reactivity of metal surfaces. Surf Sci 343(3):211–220
75. Hammer BJKN, Nørskov JK (2000) Theoretical surface science and catalysis—calculations and concepts. Adv Catal 45:71–129
76. Zhang J, Cheng L, Ma L, Sang S, Xu L, Jiang Y (2022) SiS_2 monolayer: an auspicious alkali-ion anode material with high specific capacity and ultrafast ion diffusion. Physica E 144:115474
77. Nair AK, Da Silva CM, Amon CH (2022) Tuning the adsorption and diffusion capabilities of titanium disulfide monolayers by doping and strain engineering: implications for lithium-ion batteries. Appl Surf Sci 600:154164
78. Li J, Tritsaris GA, Zhang X, Shi B, Yang C, Liu S et al (2020) Monolayer honeycomb borophene: a promising anode material with a record capacity for lithium-ion and sodium-ion batteries. J Electrochem Soc 167(9):090527
79. Samad A, Shafique A, Shin Y (2017) Adsorption and diffusion of mono, di, and trivalent ions on two-dimensional TiS_2. Nanotechnology 28(17):175401
80. Surila LX, Su S, Zhang B, Gong J (2025) Doping at sp^2-site in graphene+ monolayers as high-capacity nodal-line semimetal anodes for Na-ion batteries: a DFT study. ACS Omega 10(9):9301–9313

Publisher's Note Springer Nature remains neutral with regard to jurisdictional claims in published maps and institutional affiliations.